Phase Synchronization Method Based on Self-Oscillation Mode for Bidirectional EC-WPT System

Min Sun, Xin Dai, *Member, IEEE*, Pengqi Deng, Shijun Zhao, and Yanling Li

***Abstract*—Bidirectional electric-field coupled wireless power transfer (EC-WPT) technology with bilateral physical isolation enables energy interaction between electrical devices. Phase desynchronization of the output voltages generated by the primary and secondary converters causes issues such as periodic variations in the relative phase difference and continuous oscillations in the output power. Therefore, this article proposes a phase synchronization method based on self-oscillation mode that can tolerate misalignment of coupling plates in the bidirectional EC-WPT system. The method analyzes the effect of coupling capacitances variation on the soft-switching operating points by establishing a stroboscopic mapping model of the system, and provides a stable resonant frequency operating at the maximum amplitude-frequency gain. Based on the principle of self-oscillation, the system autonomously drives the bilateral converters by tracking the zero-crossing points of the resonant currents and ultimately operates at a stable resonant frequency for precise phase synchronization. It operates without the need for complicated computation, additional complex analog circuits, and is not affected by the variation of coupling capacitances. The experimental results show good agreement with the simulation results, validating that the effectiveness of the proposed phase synchronization method for the bidirectional EC-WPT system.**

***Index Terms*—Bidirectional wireless power transfer, electric-field coupling, phase synchronization, self-oscillation.**

I. Introduction

ELECTRIC coupled wireless power transfer (EC-WPT) technology utilizes high-frequency electric field as energy transfer carriers, and comprehensively utilizes power electronics technology, electrical theory, and modern control theory to achieve power transfer technology without direct electrical connection between power source and load [1]. EC-WPT technology solves the problem of unsafe and inflexible connection of traditional cable unplugging and wiring, and has the characteristic of power transmission through metal obstacles. EC-WPT system adopts metal plates as the coupling structure, which has the characteristics of light weight, low cost, variable shape, and low eddy current loss [2], [3], [4].

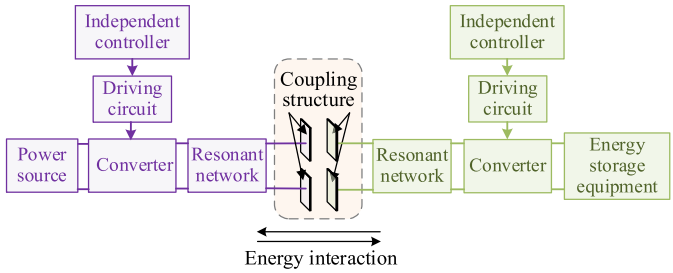

Fig. 1. Typical structural block diagram of the bidirectional EC-WPT system.

However, with the continuous expansion of the application field of EC-WPT technology, the need for bidirectional power flow of wireless electrical devices has emerged, such as vehicle to grid and battery to battery. However, traditional unidirectional EC-WPT technology cannot satisfy the energy interaction between power source and direct-current (dc) battery energy storage devices. Therefore, the unidirectional power transmission of EC-WPT system is transforming to bidirectional power transmission [5], [6]. Bidirectional EC-WPT technology can achieve bidirectional power flow between electrical devices. As a distributed energy storage device, electrical devices can provide standby power for the others, flexibly deploy the energy, increase the utility value, and facilitate energy interaction and optimal utilization between electrical devices [7], [8].

The structural block diagram of a typical bidirectional EC-WPT system is shown in Fig. 1, which consists of bidirectional converters, resonant networks, coupling structure, power source, and battery energy storage equipment.

At present, the research on the bidirectional EC-WPT technology is in the infancy. Current achievements are mainly based on the analysis and study of the phase-shifting power flow regulation method for bidirectional EC-WPT system with the typical bilateral symmetrical full-bridge converters, the magnitude and direction of the transmitted power can be regulated by the magnitude and relative phase difference between the

Received 13 July 2024; revised 28 September 2024 and 11 November 2024; accepted 15 November 2024. Date of publication 19 November 2024; date of current version 26 February 2025. This work was supported in part by the National Natural Science Foundations of China under Grant 52277003 and Grant 51977178, and in part by the Fundamental Research Funds for the Central Universities under Grant 2024CDJXY027. Recommended for publication by Associate Editor J. Biela. *(Corresponding author: Xin Dai.)*

Min Sun is with the Electrical and Automation Engineering, East China Jiaotong University, Nanchang, Jiangxi 330013, China.

Xin Dai and Shijun Zhao are with the Automation, Chongqing University, Chongqing 400044, China (e-mail: daixin@cqu.edu.cn).

Pengqi Deng is with the Optoelectronics Engineering, Chongqing University of Posts and Telecommunications, Chongqing 400065, China.

Yanling Li is with the Electrical Engineering and Electronics Information, Xihua University, Chengdu, Sichuan 610039, China.

Color versions of one or more figures in this article are available at https://doi.org/10.1109/TPEL.2024.3502249.

Digital Object Identifier 10.1109/TPEL.2024.3502249

output voltages of the primary and secondary converters [9], [10]. However, due to the fact that two independent controllers are usually utilized for the primary and secondary sides of bidirectional EC-WPT system with bilateral physically isolation in the engineering practice. Phase desynchronization of the output voltages generated by the primary and secondary converters will result in periodic variations of the relative phase difference and sustained oscillations of power [11]. In addition, since the operating frequency of bidirectional EC-WPT system is usually MHz and above to reduce the size and volume of compensation inductance, the precision of phase synchronization needs to be controlled at the level of μs or even ns in the high-frequency environment. However, the traditional wireless communication techniques have high latency and are susceptible to electromagnetic interference, which affects the precision and stability of phase synchronization in bidirectional EC-WPT system.

Some theoretical studies on phase synchronization methods of the bidirectional wireless power transfer system without any wireless communication have been reported in the past. Thrimawithana et al. [12] proposed a phase synchronization method based on the detection of voltage signal in the auxiliary windings, which synchronizes the primary resonant voltage signal by the induced voltage derived from the magnetic field generated by the primary resonant current. However, additional auxiliary winding and PLL or VCO increase the complexity of circuit design. Tian et al. [13] proposed a synchronization strategy based on power-phase angle perturbation independent of adding additional circuit, and the desired power can be achieved by interfering with the relative phase difference. However, the power fluctuates continuously under the disturbance of the relative phase difference, which affects the stability of the system. On the other hand, Zhang et al. [14] and Liu et al. [15] proposed synchronization control methods by periodically detecting and tracking the extreme value of the output current to correct the relative phase difference, respectively. Such solutions reduce the complexity and cost of the system. However, the aforementioned former control strategies cannot be implemented in case of changing system parameters. Although the latter control strategy can effectively overcome the misalignment tolerance of the coupling structure, the robustness of the system is poor due to the nonreal-time sampling of the current detection. Tang et al. [16] proposed a zero reactive power control technique. Although the strategy can overcome misalignment of coupling coils, it requires complex hardware circuits (multiplier, phase shifter, and low-pass filter), which may lead to inaccurate detection and adverse to the stable operation of bidirectional EC-WPT system in the high-frequency environment.

The aforementioned phase synchronization methods are oriented to bidirectional magnetic-filed coupling WPT system using magnetic fields as energy carrier, with an operating frequency of around kHz, whereas the frequency of bidirectional EC-WPT systems is usually MHz or above. Thus, the precision of phase synchronization needs to be controlled at the level of μs or even ns in a high-frequency environment. This article proposes a simple and reliable method that achieves precise phase synchronization at μs level between primary and secondary sides of bidirectional EC-WPT system without any wireless communication. The overall comparison of aforementioned phase synchronization methods and the proposed method in terms of additional circuit, design complexity, and real-time sampling is shown in Table I. The proposed phase synchronization method based on self-oscillation mode is not complicated computation, additional analog circuit, and unaffected by variation on coupling capacitances, the only hardware requirements of the proposed method are the current detection circuit. The experimental results of the bidirectional EC-WPT system show that the proposed phase synchronization method is feasible and applicable.

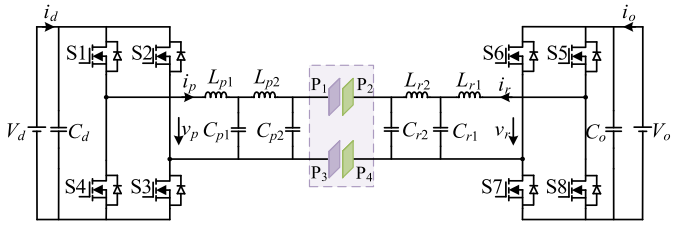

Fig. 2. Circuit diagram of dual *LCLC*-compensated bidirectional EC-WPT system.

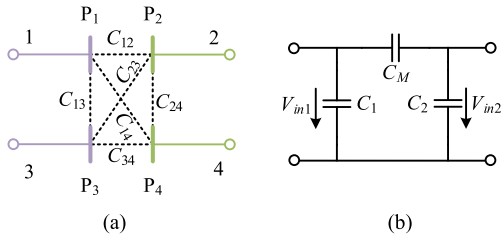

Fig. 3. Equivalent π model of coupling capacities. (a) Four-plates capacitance model. (b) Equivalent current source model.

II. Topology and Modeling of Bidirectional EC-WPT System

In this article, bilateral *LCLC*-compensated bidirectional EC-WPT system is shown in Fig. 2. Due to the advantages of *LCLC* resonant network in reducing the current and voltage stresses on the circuit components near the coupling plates, as well as the proportionality between the output power and the coupling coefficient [17]. Coupling exists between every two plates, resulting in six capacitances C_{12}–C_{34}, as shown in Fig. 3. P_1 and P_3 are embedded in the primary side, while P_2 and P_4 are placed at the secondary side. The coupling capacitances are simplified to the equivalent π model, which is suitable to simplify the parameter calculation in the circuit. Thus, Fig. 4 shows a simplified circuit diagram of the equivalent π model for the bidirectional EC-WPT system, and the coupling capacitances can be expressed as

$$\begin{cases} C_1 = C_{p2} + C_{x1} - C_M \\ C_2 = C_{r2} + C_{x2} - C_M \end{cases} \tag{1}$$

TABLE I
COMPARISON OF CRITICAL CHARACTERISTICS OF PHASE SYNCHRONIZATION METHODS

Paper	Synchronization Method	Misalignment tolerance	Additional circuit	Design complexity	Real-time sampling	Computational complexity	Power disturbance
[12]	Auxiliary circuit	No	Yes	High	No	Medium	Yes
[13]	Power-phase angle perturbation	No	No	Medium	Yes	Medium	Yes
[14]	Output current periodic detection	No	No	Low	Yes	Low	No
[15]	Output current extreme tracking	Yes	No	Medium	No	Low	No
[16]	Zero reactive power control	Yes	No	Medium	Yes	High	No
This work	Self-oscillation	Yes	No	Low	Yes	Low	No

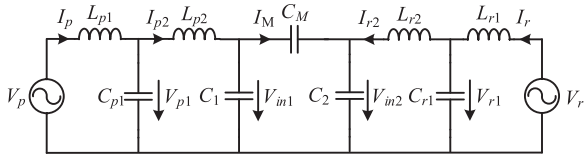

Fig. 4. Simplified circuit with equivalent π model of the proposed bidirectional EC-WPT system.

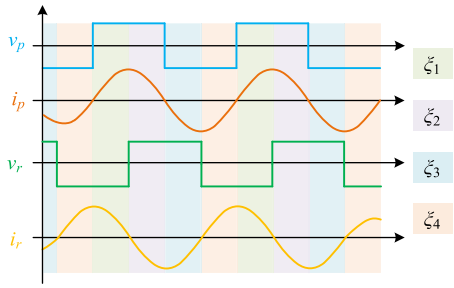

Fig. 5. Resonant voltages and currents waveforms of the primary and secondary side converters.

where

$$\begin{cases} C_{x1} = C_{13} + \frac{(C_{12}+C_{14})(C_{23}+C_{34})}{C_{12}+C_{14}+C_{23}+C_{34}} \\ C_{x2} = C_{24} + \frac{(C_{12}+C_{23})(C_{14}+C_{34})}{C_{12}+C_{14}+C_{23}+C_{34}} \\ C_M = \frac{C_{12}C_{34}-C_{14}C_{23}}{C_{12}+C_{14}+C_{23}+C_{34}}. \end{cases} \tag{2}$$

According to KVL's law, the differential equation for the equivalent π model of the system shown in Fig. 4 can be expressed as

$$\begin{cases} \frac{di_p}{dt} = \frac{1}{L_{p1}}u_p - \frac{1}{L_{p1}}u_{p1} \\ \frac{du_{p1}}{dt} = \frac{1}{C_{p1}}i_p - \frac{1}{C_{p1}}i_{p2} \\ \frac{di_{p2}}{dt} = \frac{1}{L_{p2}}u_{p1} - \frac{1}{L_{p2}}u_{in1} \\ \frac{du_{in1}}{dt} = \frac{C_{in2}}{C_{in1}C_{in2}-C_M^2}i_{p2} + \frac{C_M}{C_{in1}C_{in2}-C_M^2}i_{r2} \\ \frac{du_{in2}}{dt} = \frac{C_M}{C_{in1}C_{in2}-C_M^2}i_{p2} + \frac{C_{in1}}{C_{in1}C_{in2}-C_M^2}i_{r2} \\ \frac{di_{r2}}{dt} = \frac{1}{L_{r2}}u_{r1} - \frac{1}{L_{r2}}u_{in2} \\ \frac{du_{r1}}{dt} = \frac{1}{C_{r1}}i_r - \frac{1}{C_{r1}}i_{r2} \\ \frac{di_r}{dt} = \frac{1}{L_{r1}}u_r - \frac{1}{L_{r1}}u_{r1}. \end{cases} \tag{3}$$

$x = [i_p \ u_{p1} \ i_{p2} \ u_{in1} \ u_{in2} \ i_{r2} \ u_{r1} \ i_r]$ is the state vector of the system and $u = [u_p \ \ u_r]^T$ is the input vector. So, the state space model can be expressed as

$$\dot{x} = \mathbf{A}x + \mathbf{B}u \tag{4}$$

where $\mathbf{A}$ is the system coefficient matrix, $\mathbf{B}$ is the system input matrix, and can be derived as

$$\mathbf{A} = \begin{bmatrix} 0 & -\frac{1}{L_{p1}} & 0 & 0 & 0 & 0 & 0 & 0 \\ \frac{1}{C_{p1}} & 0 & -\frac{1}{C_{p1}} & 0 & 0 & 0 & 0 & 0 \\ 0 & \frac{1}{L_{p2}} & 0 & -\frac{1}{L_{p2}} & 0 & 0 & 0 & 0 \\ 0 & 0 & \frac{C_{in2}}{\Delta} & 0 & 0 & \frac{C_M}{\Delta} & 0 & 0 \\ 0 & 0 & \frac{C_M}{\Delta} & 0 & 0 & \frac{C_{in1}}{\Delta} & 0 & 0 \\ 0 & 0 & 0 & 0 & -\frac{1}{L_{r2}} & 0 & \frac{1}{L_{r2}} & 0 \\ 0 & 0 & 0 & 0 & 0 & -\frac{1}{C_{r1}} & 0 & \frac{1}{C_{r1}} \\ 0 & 0 & 0 & 0 & 0 & 0 & -\frac{1}{L_{r1}} & 0 \end{bmatrix} \tag{5}$$

$$\mathbf{B} = \begin{bmatrix} \frac{1}{L_{p1}} & 0 & 0 & 0 & 0 & 0 & 0 & 0 \\ 0 & 0 & 0 & 0 & 0 & 0 & 0 & \frac{1}{L_{r1}} \end{bmatrix}^T \tag{6}$$

where

$$\Delta = C_{in1}C_{in2} - C_M^2. \tag{7}$$

According to the turn-ON and turn-OFF states of the primary and secondary converter switches can be linearized into four modes, the resonant voltages and currents waveforms are shown in Fig. 5, and four modes can be given as follows.

1) Mode I: Switches S1, S3, S6, and S8 turn-ON, S2, S4, S5, and S7 turn-OFF, $u_p = E_d, u_r = -E_o, u_1 = [E_d \ -E_o]^T$, and the steady-state duration is ξ_1.
2) Mode II: Switches S1, S3, S5, and S7 turn-ON, S2, S4, S6, and S8 turn-OFF, $u_p = E_d, u_r = E_o, u_2 = [E_d \ E_o]^T$, and the steady-state duration is ξ_2.
3) Mode III: Switches S1, S3, S6, and S8 turn-OFF, S2, S4, S5, and S7 turn-ON, $u_p = -E_d, u_r = E_o, u_3 = [-E_d \ E_o]^T$, and the steady-state duration is ξ_3.
4) Mode IV: Switches S1, S3, S5, and S7 turn-OFF, S2, S4, S6 and S8 turn-ON, $u_p = -E_d, u_r = -E_o, u_4 = [-E_d \ -E_o]^T$, and the steady-state duration is ξ_4.

Supposing steady-state operating period of the system is T_ξ, and the operating duration of each linear mode is ξ_i, then

$$T_\xi = \sum_{i=1}^{k} \xi_i \quad (k = 4). \tag{8}$$

Thus, the voltage source u can be expressed as

$$u = \begin{cases} [E_d \quad -E_o]^T, & t \in [0, \xi_1) \\ [E_d \quad E_o]^T, & t \in [\xi_1, \xi_1 + \xi_2) \\ [-E_d \quad E_o]^T, & t \in [\xi_1 + \xi_2, \xi_1 + \xi_2 + \xi_3) \\ [-E_d \quad -E_o]^T, & t \in (\xi_1 + \xi_2 + \xi_3, T_\xi]. \end{cases} \tag{9}$$

The state mapping function of each mode is obtained as

$$\begin{aligned} f_{i,\xi_i}(x) = {} & \mathbf{\Phi}_i(\xi_i)\, x + (\mathbf{\Phi}_i(\xi_i) - I) \\ & \times \mathbf{A}_i{}^{-1}\mathbf{B}_i u_i \quad (i = 1, 2, 3, 4) \end{aligned} \tag{10}$$

where

$$\mathbf{\Phi}_i(\xi_i) = e^{\mathbf{A}_i \xi_i} \qquad (i = 1, 2, 3, 4). \tag{11}$$

Supposing x_n is the periodic initial state when the system is in steady state, while x_{n+1} is the periodic end state, then the stroboscopic mapping model for the nth operating cycle of the system can be expressed as

$$\begin{aligned} x_{n+1} &= f_{4,\xi_4} \circ f_{3,\xi_3} \circ f_{2,\xi_2} \circ f_{1,\xi_1}(x_n) \\ &= \mathbf{\Phi}_4(\xi_4)\, \mathbf{\Phi}_3(\xi_3)\, \mathbf{\Phi}_2(\xi_2)\, \mathbf{\Phi}_1(\xi_1)\, x_n + \mathbf{\Phi}_4(\xi_4) \\ &\quad \mathbf{\Phi}_3(\xi_3)\, \mathbf{\Phi}_2(\xi_2)\, (\mathbf{\Phi}_1(\xi_1) - \mathbf{I})\, \mathbf{A}^{-1}\mathbf{B} u_1 + \mathbf{\Phi}_4(\xi_4) \\ &\quad \mathbf{\Phi}_3(\xi_3)\, (\mathbf{\Phi}_2(\xi_2) - \mathbf{I})\, \mathbf{A}^{-1}\mathbf{B} u_2 + \mathbf{\Phi}_4(\xi_4) \\ &\quad (\mathbf{\Phi}_3(\xi_3) - \mathbf{I})\, \mathbf{A}^{-1}\mathbf{B} u_3 + (\mathbf{\Phi}_4(\xi_4) - \mathbf{I})\, \mathbf{A}^{-1}\mathbf{B} u_4 \end{aligned} \tag{12}$$

where $\circ$ represents composite mapping operator, which can be defined as $f \circ g(t) = f(g(t))$.

The state vector of the system repeats periodically at steady state.

$$x_{n+1} = x_n. \tag{13}$$

Thus, x_n can be derived as

$$x_n = (\mathbf{I} - \mathbf{\Phi}(\xi_4)\, \mathbf{\Phi}(\xi_3)\, \mathbf{\Phi}(\xi_2)\, \mathbf{\Phi}(\xi_1))^{-1} \cdot \left\{ \begin{array}{l} \mathbf{\Phi}(\xi_4)\, \mathbf{\Phi}(\xi_3)\, \mathbf{\Phi}(\xi_2)\, (\mathbf{\Phi}(\xi_1) - \mathbf{I})\, \mathbf{A}^{-1}\mathbf{B} u_1 \\ \quad + \mathbf{\Phi}(\xi_4)\, \mathbf{\Phi}(\xi_3)\, (\mathbf{\Phi}(\xi_2) - \mathbf{I})\, \mathbf{A}^{-1}\mathbf{B} u_2 + \mathbf{\Phi}(\xi_4) \\ (\mathbf{\Phi}(\xi_3) - \mathbf{I})\, \mathbf{A}^{-1}\mathbf{B} u_3 + (\mathbf{\Phi}(\xi_4) - \mathbf{I})\, \mathbf{A}^{-1}\mathbf{B} u_4 \end{array} \right\}. \tag{14}$$

Since the switches ON the same side of the leg of primary and secondary converters are 180° complementary conduction, the corresponding relationship between each operating mode of the system can be obtained as

$$\xi_2 = \frac{T_\xi}{2} - \xi_1, \xi_3 = \xi_1, \xi_4 = \xi_2. \tag{15}$$

According to Fig. 5, the relative phase difference between the primary and secondary resonant voltages is defined as θ, and $V_r = V_p \angle \theta$, the relationship of θ and ξ_1 can be given as

$$\xi_1 = \frac{\theta}{2\pi} T_\xi. \tag{16}$$

Therefore, the system periodic fixed-point x^* is obtained as

$$x^* = (\mathbf{I} - \mathbf{\Phi}(T_\xi))^{-1} \cdot \left\{ \begin{array}{l} \mathbf{\Phi}\left(\frac{\pi-\theta}{2\pi} T_\xi\right) \mathbf{\Phi}\left(\frac{\theta}{2\pi} T_\xi\right) \mathbf{\Phi}\left(\frac{\pi-\theta}{2\pi} T_\xi\right) \\ \quad \left(\mathbf{\Phi}\left(\frac{\theta}{2\pi} T_\xi\right) - \mathbf{I}\right) \mathbf{A}^{-1}\mathbf{B} u_1 \\ + \mathbf{\Phi}\left(\frac{\pi-\theta}{2\pi} T_\xi\right) \mathbf{\Phi}\left(\frac{\theta}{2\pi} T_\xi\right) \left(\mathbf{\Phi}\left(\frac{\pi-\theta}{2\pi} T_\xi\right) - \mathbf{I}\right) \\ \quad \mathbf{A}^{-1}\mathbf{B} u_2 + \mathbf{A}^{-1}\mathbf{B} u_3 \\ \mathbf{\Phi}\left(\frac{\pi-\theta}{2\pi} T_\xi\right) \left(\mathbf{\Phi}\left(\frac{\theta}{2\pi} T_\xi\right) - \mathbf{I}\right) \\ \quad + \left(\mathbf{\Phi}\left(\frac{\pi-\theta}{2\pi} T_\xi\right) - \mathbf{I}\right) \mathbf{A}^{-1}\mathbf{B} u_4 \end{array} \right\}. \tag{17}$$

When T_ξ is considered as a variable, the periodic fixed-point x^* is regarded as a function of the period T_ξ. Extracting the resonant current components of the primary and secondary sides from the fixed-point x^*, the system fixed-point function used to analyze the ZCS soft-switching operating points can be obtained as

$$f_{x^*}(t) = \mathbf{C} x^*(t) \tag{18}$$

where $\mathbf{C}$ is the state selection matrix

$$\mathbf{C} = \begin{bmatrix} 1 & 0 & 0 & 0 & 0 & 0 & 0 & 0 \\ 0 & 0 & 0 & 0 & 0 & 0 & 0 & 1 \end{bmatrix}. \tag{19}$$

$\mathbf{C}_1 = \begin{bmatrix} 1 & 0 & 0 & 0 & 0 & 0 & 0 & 0 \end{bmatrix}$. and $\mathbf{C}_2 = [0 \ 0 \ 0 \ 0 \ 0 \ 0 \ 0 \ 1]$. can extract the resonant current components i_p and i_r from the state vector x, respectively.

In order to achieve ZCS soft-switching operation, i_p and i_r should satisfy the following conditions:

$$\begin{cases} i_p(t) = 0 \\ i_r(t) = 0 \end{cases}. \tag{20}$$

Thus, the ZCS soft-switching operating points can be obtained from (20).

Besides, on the basis of the equivalent circuit of the system shown in Fig. 4, the transfer function matrix $\mathbf{G}$ can be represented

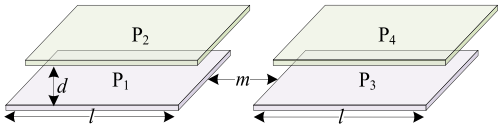

Fig. 6. Structure and dimensions of coupling plates.

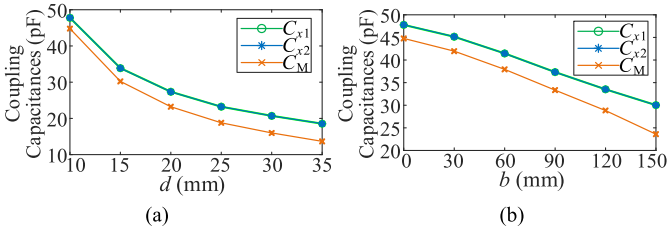

Fig. 7. Variation curves of coupling capacitances. (a) Change of transmission distance. (b) Lateral movement of the coupling plates.

as

$$\mathbf{G}(s)=\frac{\mathbf{Y}(s)}{\mathbf{U}(s)}=\mathbf{C}(s\mathbf{I}-\mathbf{A})^{-1}\mathbf{B}=\begin{bmatrix}\mathbf{G}_{11}(s) & \mathbf{G}_{12}(s)\\ \mathbf{G}_{21}(s) & \mathbf{G}_{22}(s)\end{bmatrix} \tag{21}$$

where

$$\mathbf{G}_{11}(s)=\frac{I_p(s)}{U_p(s)},\mathbf{G}_{12}(s)=\frac{I_p(s)}{U_r(s)}$$
$$\mathbf{G}_{21}(s)=\frac{I_r(s)}{U_p(s)},\mathbf{G}_{22}(s)=\frac{I_r(s)}{U_r(s)}. \tag{22}$$

According to (22), the magnitude-frequency and phase-frequency relationship curves of each element in the transfer function matrix can be obtained.

III. Analysis of Coupling Capacitances Variation and System Frequency Characteristics

A. Analysis of Changing in Coupling Capacitances

In practical applications, the position or the transmission distance of wireless electrical devices based on the bidirectional EC-WPT system will inevitably change, resulting in random changes in the coupling capacitances. In order to simplify the analysis, this article adopts the parallel structure of the coupling plates, and the specific dimensions are shown in Fig. 6, where the length l of the coupling plates P_1–P_4 is 300 mm, the thickness of all plates is 2 mm, the transmission distance is d, the distance between P_1-P_2 and P_3-P_4 is m.

Through the finite element simulation software of Maxwell, Fig. 7 shows the variation curves of the coupling self-capacitances C_{x1}, C_{x2} and equivalent mutual capacitance C_M when the coupling plates is lateral movement or the transmission distance changes. Where Fig. 7(a) shows the variation curves of coupling self-capacitance and equivalent mutual-capacitance with transmission distance d in the absence of lateral movement of the coupling plates; Fig. 7(b) shows the variation curves of the coupling self-capacitances and equivalent mutual-capacitance with the lateral movement distance b of the coupling plates under the transmission distance d of 10 mm. It can be obtained from the simulation results that C_{x1}, C_{x2}, and C_M decrease continuously with the increasing of b or d. The trend of C_{x1} and C_{x2} are consistent, which is due to the fact that the lateral movement of the coupling plates and the change in transmission distance have the same impact on the two coupling self-capacitances in the symmetrical parallel structure of the coupling plates.

TABLE II
Parameters of the System

Parameter	Value	Parameter	Value
$E_d(V)$	100	E_o(V)	100
$L_{p1}(\mu H)$	25	$L_{p2}(\mu H)$	150
$L_{r1}(\mu H)$	25	$L_{r2}(\mu H)$	150
C_{p1}(nF)	1.184	C_{p2}(pF)	149.2
C_{r1}(nF)	1.184	C_{r2}(pF)	149.2

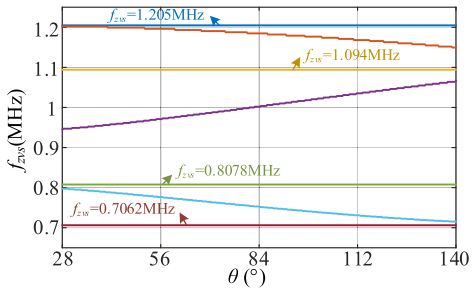

Fig. 8. Curves of ZCS soft switching frequencies varies with relative phase difference while d is 10 mm.

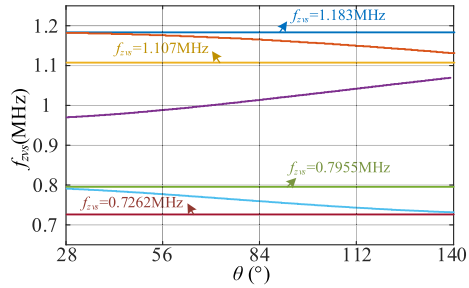

Fig. 9. Curves of ZCS soft switching frequencies varies with relative phase differences while d is 15 mm.

B. System Resonance Frequency Analysis

Due to the coupling capacitances vary with lateral movement of the coupling plates or change in transmission distance. In order to analyze the effect on the multiple soft-switching operating points of the system under the variation of the coupling capacitances, the parameters of the system are shown in Table II, where the parameters of the resonant network are set as symmetric.

Taking the change in transmission distance as an example, according to the parameters shown in Table II and (20), Figs. 8 and 9 show the curves of multiple soft-switching operating points under the change of relative phase difference θ for two cases of $d = 10$ mm and 15 mm, respectively. It can be seen from Fig. 8 that the ZCS frequency points changes accordingly

and the system contains 7 ZCS soft-switching operating points under changes in the relative phase difference θ when d is 10 mm. Meanwhile, four of the soft-switching operating points remain constant with the change of θ, corresponding to the four resonant frequency points of 0.7062 MHz, 0.8078 MHz, 1.094 MHz, and 1.205 MHz, respectively. Similar to Fig. 8, when the coupling transmission distance d is 15 mm, as shown in Fig. 9, the four resonant frequency points of 0.7262 MHz, 0.7955 MHz, 1.107 MHz, and 1.183 MHz, respectively. Thus, it can be seen that even though the coupling capacitances change, the trend of the ZCS soft-switching operating points is the same, but the corresponding ZCS soft-switching operating points are changing due to the change of the coupling capacitances.

Besides, due to the circuit parameters of the primary and secondary sides of the system are completely symmetrical, the soft-switching operating points corresponding to the zero-crossing points of the primary resonant current given in Figs. 8 and 9 are exactly the same as the soft-switching operating points corresponding to that of the secondary resonant current.

Based on the abovementioned analysis, it can be seen that the system has multiple ZCS soft-switching operating points under the given circuit parameters. And the resonant frequency points of the system are those soft-switching operating points where the driving frequency coincides with the oscillation frequency [18]. When the system operates in self-oscillation mode, the bilateral independent controllers switch the converters in real time according to the zero-crossing signal of the circuit, and ultimately operates at a stable resonant frequency, and eventually converge to the point with the highest output gain of the magnitude-frequency [19].

Therefore, according to (21) and (22) and the parameters of Table II, the magnitude and phase plots of each element in the transfer function matrix $\mathbf{G}$ at $d = 10$ mm are given, as shown in Fig. 10, and the maximum gain point of the system is at the resonant frequency of 0.8078 MHz. Meanwhile, Fig. 11 shows the amplitude-frequency and phase-frequency plots at $d = 15$ mm, the maximum gain point of the system is at the resonant frequency of 0.7955 MHz. Due to the system structure and parameters are completely symmetric, $\mathbf{G}_{11}$ is similar to $\mathbf{G}_{22}$, and $\mathbf{G}_{12}$ is similar to $\mathbf{G}_{21}$.

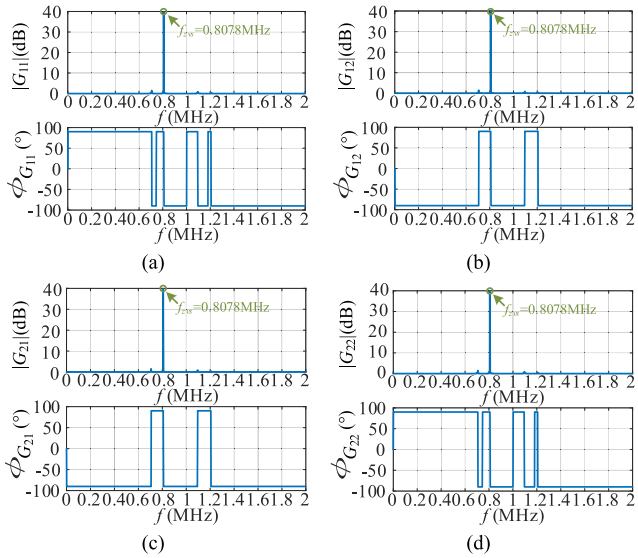

Fig. 10. Magnitude-frequency and phase-frequency curves of system transfer function matrix while d is 10 mm. (a) Primary resonant current and voltage. (b) Primary resonant current and secondary resonant voltage. (c) Secondary resonant current and primary resonant voltage. (d) Secondary resonant current and voltage.

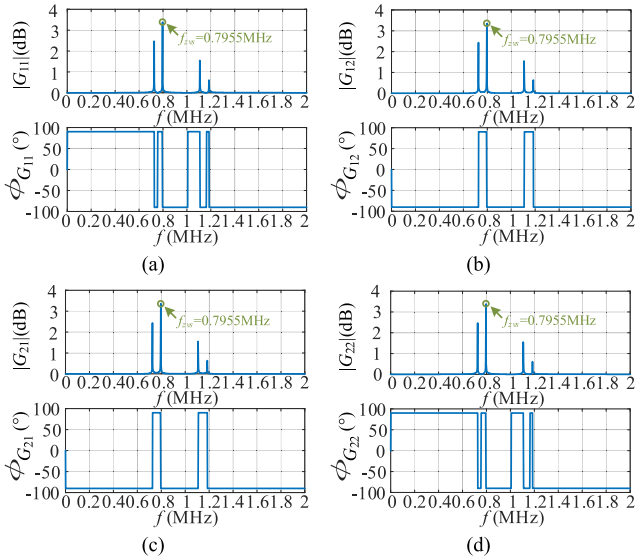

Fig. 11. Magnitude-frequency and phase-frequency curves of system transfer function matrix while d is 15 mm. (a) Primary resonant current and voltage. (b) Primary resonant current and secondary resonant voltage. (c) Secondary resonant current and primary resonant voltage. (d) Secondary resonant current and voltage.

IV. Phase Synchronization Method

Through the analysis in Section III, it can be concluded that the self-oscillation system will eventually converge automatically to the resonant frequency point with the largest amplitude-frequency gain, and the system can operate to the corresponding stable resonant frequency point even when the coupling capacitances change. Therefore, a phase synchronization method based on self-oscillation mode, which is applicable to the variation on coupling capacitances is proposed for the bidirectional EC-WPT system with bilateral *LCLC* resonant networks, as shown in Fig. 12. The control circuit of the phase synchronization method consists of the current detection circuit, logic control circuit and driving circuit. The current detection circuit uses a current transformer to sample the resonant currents of the primary and secondary sides, and the sampled current signals are fed to the zero-crossing comparator, which convert the resonant currents into the square-wave synchronization signals with a duty cycle of 50%. The logic control circuit is divided into two logic signals, one is the driving signal of the initial frequency during the startup stage; Another is the control signal to drive the switches based on the zero-crossing resonant current.

The circuit schematic of the phase synchronization method is shown in Fig. 13, where Fig. 13(a) and (b) is the primary and secondary resonant current sampling circuits, respectively.

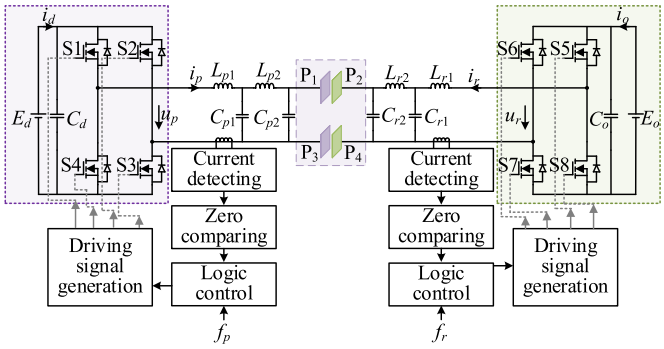

Fig. 12. Block diagram of the phase synchronization method for the dual *LCLC* resonant network bidirectional EC-WPT system.

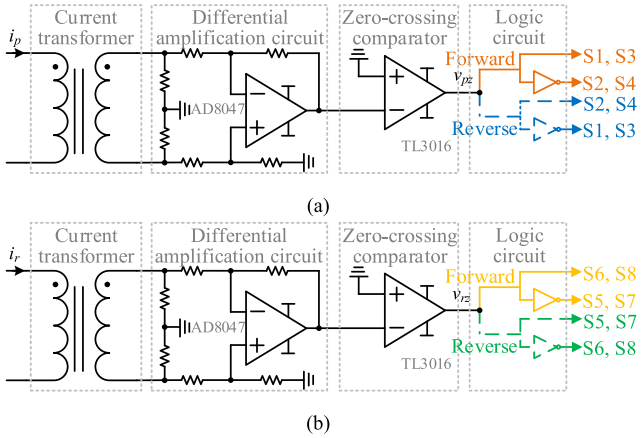

Fig. 13. Schematic circuit diagram of the self-oscillation phase synchronization method. (a) Primary side. (b) Secondary side.

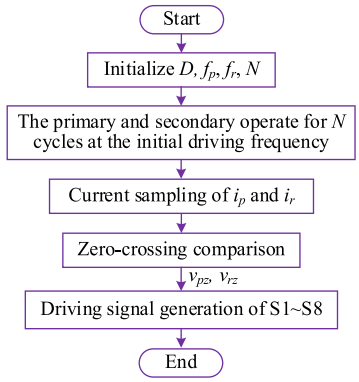

Fig. 14. Flowchart of the phase synchronization method.

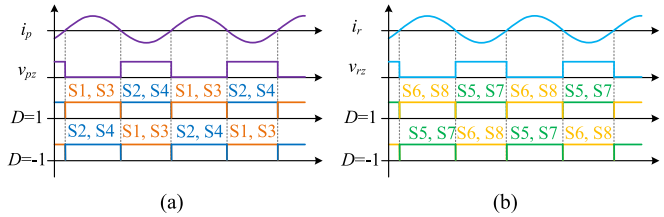

Fig. 15. Primary and secondary resonant currents, square wave synchronization voltage driving signals and switches driving sequences. (a) Primary side. (b) Secondary side.

During the power-ON startup stage, the primary and secondary converters are driven according to the given initial operating frequency, and the system starts to self-oscillate after a period of fixed-frequency operation. At this time, the controller detects the zero-crossing point of the square-wave voltage signal generated by the resonant current passing through the zero-crossing comparator, the state of the primary and secondary switches changes accordingly, and each branch operates with a duty cycle of approximately 50%. Finally, the relative phase difference of the resonant voltages on the primary and secondary sides remains constant, and the resonant currents no longer oscillate periodically, the resonant voltages and currents of primary and secondary converters remain in the same phase, and the system operates at a stable resonant frequency point, achieving phase synchronization of the system.

The control flowchart of the proposed phase synchronization method for the bidirectional EC-WPT system is shown in Fig. 14, and the specific procedures are as follows.

1) Initialize the power transmission direction D, the initial driving frequencies f_p and f_r of the primary and secondary converters, and the fixed-frequency operating cycle N.
2) The primary and secondary controllers operate for N cycles at initial operating frequency f_p and f_r, respectively.
3) After the system operated for N cycles, the sampled primary resonant current i_p passes through the primary zero-crossing comparator to obtain the square wave voltage signal v_{pz}, and the sampled secondary resonant current i_r passes through the secondary zero-crossing comparator to obtain the square wave synchronized voltage signal v_{rz}.
4) The primary and secondary controllers generate the driving signals of switches S1–S8 based to the power transmission direction and synchronous voltage signals.

Define forward power transfer of the system when $D = 1$, and reverse power transfer when $D = -1$. The synchronization voltage driving signal and switches driving sequence diagram of the proposed phase synchronization method based on self-oscillation modeare shown in Fig. 15. Among them, Fig. 15(a) shows the driving waveforms of the primary resonant current i_p, the synchronizing voltage signal v_{pz} output from the zero-crossing comparator and the switches S1–S4, while Fig. 15(b) shows the driving waveforms of the secondary resonant current i_r, the synchronizing voltage signal v_{rz} output by the zero-crossing comparator and the switches S5–S8.

1) When $D = 1$, the primary converter is regarded as an inverter and the secondary converter as a synchronous rectifier. When the system performs self-oscillation phase synchronization, a square-wave synchronous voltage signal is output after sampling the resonant current and zero-crossing comparison to drive the switches. The primary controller controls the drive signals of the switches S1 and S3 to be in phase with the synchronized voltage signal v_{pz}, S2 and S4 to be in inverse phase with v_{pz}; The secondary controller controls the drive signals of S6 and S8 to be in

phase with the synchronized voltage signal v_{rz}, S5 and S7 to be in inverse phase with v_{rz}.

2) When $D = -1$, the secondary converter is regarded as an inverter and the primary converter as a synchronous rectifier. When the system performs self-oscillation phase synchronization, the switches are driven according to the square wave synchronization signal output from the zero-crossing comparison of the sampled current. The primary controller controls the drive signals of S2 and S4 to be in phase with v_{pz}, S1 and S3 to be in inverse phase with v_{pz}; The secondary controller controls the drive signals of S5 and S7 are to be phase with v_{rz}, S6 and S8 to be in inverse phase with v_{rz}.

In order to achieve precise current detection in a high-frequency environment, several aspects are worth to be noting as follows.

1) *Common-Mode Interference*. To reduce the impact of common-mode interference on the detection circuit, a symmetrical impedance network is adopted at the input of the detection circuit, and the amplification of the measured signal is achieved through a differential amplification circuit. An isolated power supply with high resistance to common-mode interference is used in the power supply of the entire detection circuit, and the signal is transmitted in isolation through a digital signal isolator.
2) *Reliable Current Detection Under Low Transmission Power*. Since the voltage comparator needs to realize a low-delay output voltage logic trigger, and the amplitude of the input signal should be greater than a certain overdrive threshold. Besides, when the transmission power of the system is small, the high-frequency current of the converter may be relatively small. Therefore, signal amplification in the detection circuit is necessary.
3) *Signal Transmission Delay*. Although high-frequency devices were selected, the accumulated signal transmission delay due to the composition of multiple signal processing circuits will inevitably affect the operation of the system at high frequency. Therefore, an *RC* lead compensation network is added to the detection circuit so that the stability of the lead-time of the *RC* lead compensation network will not be significantly affected even though the system operates in the frequency range of around MHz.

V. Experimental Results

In order to verify the feasibility of the proposed phase synchronization method, an experimental setup is constructed shown in Fig. 16. The system consists of primary and secondary full-bridge converters controlled by two independent controllers, and the converters using GaN power modules operates at a switching frequency of MHz.

This article adopts a reliable high-speed signal detection scheme to control the precision at accurate frequency, which mainly includes the conversion link from high-frequency current of the converter to voltage signal, voltage signal amplification processing, and high common-mode interference isolation power supply. The high-frequency current transformer

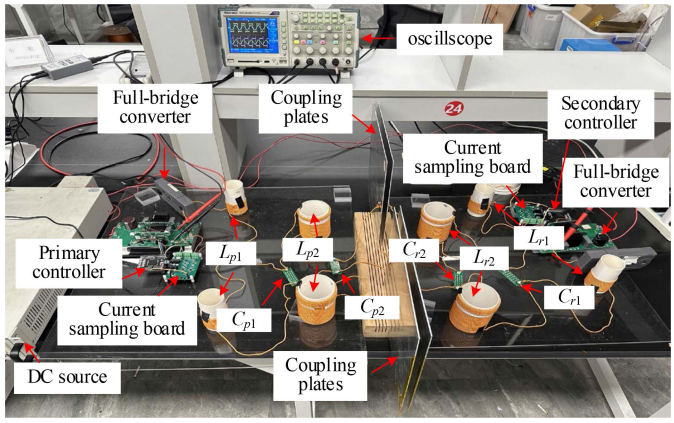

Fig. 16. Experiment setup.

(CU8965-AL) realizes the conversion of current to voltage signals, and the operating frequency range of the current transformer reaches to 1 MHz and above. In addition, a high-speed voltage comparator (TL3016) is utilized to improve the accuracy of the detection of the zero-crossing current, and the propagation delay of the signal is 7.6 ns, which is much smaller than the period of the measured current. Besides, the high-speed operational amplifier (AD8047) with sufficient bandwidth is selected to reduce the detection error caused by high-frequency signals, which has a bandwidth of 325 MHz and slew rate of 1000 V/μs.

The experimental prototype adopts the circuit parameters in Table II. The primary and secondary parallel compensation capacitors C_{r1}, C_{r2}, C_{p1}, and C_{p2} use SMD ceramic capacitors. The primary and secondary compensation inductors L_{r1}, L_{r2}, L_{p1}, and L_{p2} are wrapped around PVC pipes with Litz wires.

In order to compare with theoretical modeling and simulation analysis, the phase synchronization method based on self-oscillation mode of the bidirectional EC-WPT system is experimentally verified for the two case of transmission distances of 10 mm and 15 mm, respectively, and the dynamic response and waveforms of the system tolerating misalignment of coupling plates from phase desynchronization to synchronization. The system transmission power is first set to be forward, i.e., $D = 1$, and the initial fixed operating frequencies f_p and f_r of the primary and secondary converters are 1 MHz. In the initial stage, the primary and secondary converters are driven at the initial frequency of 1 MHz, the system is in phase desynchronization due to the natural physical isolation of primary and secondary sides. After the system operates at a fixed frequency for a period of time, the primary and secondary converters autonomously by tracking the zero-crossing points of the resonant currents and ultimately operates at a stable resonant frequency, thereby achieving phase synchronization of the system.

The experimental waveforms of self-oscillation phase synchronization for the system at the coupling transmission distance of 10 mm are shown in Fig. 17, where the resonant voltage and resonant current of the primary side are v_p and i_p, respectively, and the resonant voltage and resonant current of the secondary side are v_r and i_r, respectively. Fig. 17(a) is a complete view of the dynamic respond switching from fixed frequency drive

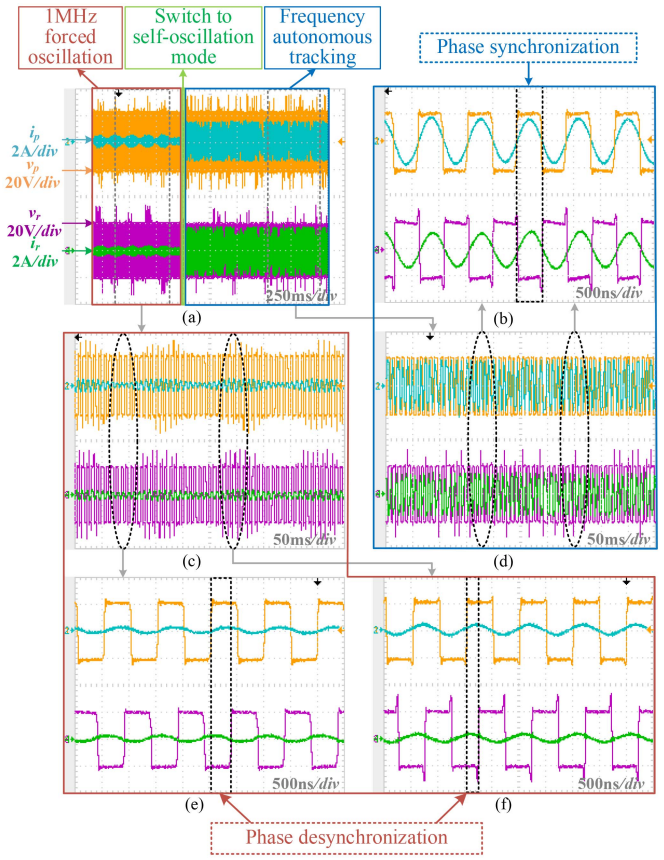

Fig. 17. Experimental waveforms of phase synchronization of the system at the transmission distance of 10 mm. (a) Complete view of the envelopes of v_p, i_p, v_r and i_r. (b) Enlarged view of the self-oscillation in Fig. 17(d). (c) Enlarged view of the fixed-frequency drive stage in Fig. 17(a). (d) Enlarged view of the self-oscillation in Fig. 17(a). (e) Unfolded views at one of the moments in Fig. 17(c). (f) Unfolded views at one of the moments in Fig. 17(c).

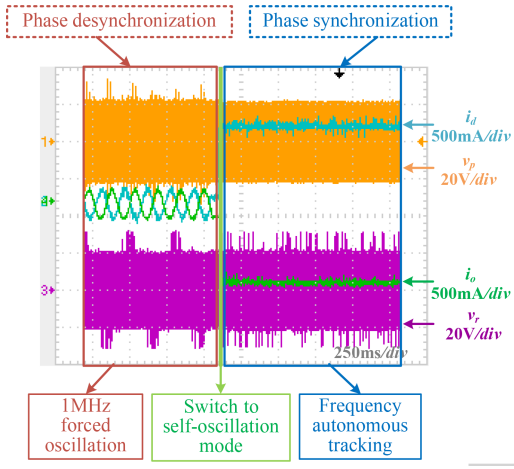

Fig. 18. Experimental waveforms of the dc output currents.

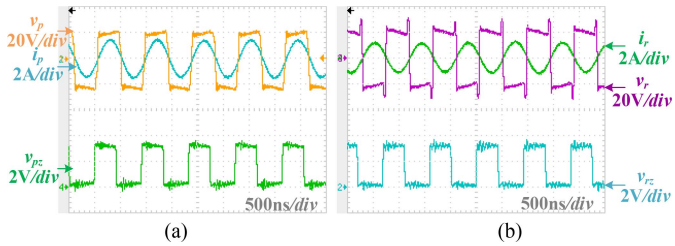

Fig. 19. Experimental waveforms of the resonant voltage, resonant current, and the square wave synchronization signal of primary and secondary of the system. (a) Primary resonant voltage and current, the square wave synchronization signal of primary side. (b) Secondary resonant voltage and current, the square wave synchronization signal of secondary side.

to resonant frequency tracking autonomously. From which it can be seen that the primary and secondary converters are first driven at the given initial frequency, and after the system operates at a fixed frequency for a period of time, the system switches to self-oscillation mode, the primary and secondary converters autonomously follow the synchronized voltage square-wave signals after the zero-crossing comparison of the resonant current, thereby achieving phase synchronization of the system, and the system ultimately operates at a stable resonant frequency. Fig. 17(c) is an enlarged view of the fixed-frequency drive stage in Fig. 17(a), showing that the system drives the primary and secondary converters at an initial frequency of 1 MHz during the initial fixed-frequency startup stage, and at this time, the resonant currents of the primary and secondary sides oscillate periodically. Fig. 17(e) and (f) is the unfolded views at any two moments in Fig. 17(c), it can be seen more intuitively that the relative phase difference between the primary and secondary resonant voltages of the system constantly changes during the fixed-frequency startup stage. At this time, the primary resonant voltage and current are not in/antiphase, and the secondary is also not in/antiphase, so the system phase is not synchronized. Fig. 17(d) and (b) is the enlarged views of the self-oscillation stage of the system in Fig. 17(a), showing that the system achieves phase synchronization by following the zero-crossing points of the resonant currents to self-excited drive the converters, the resonant current of the primary and secondary sides remains stable, the relative phase difference keeps constant, and the resonant voltage and current of the primary (secondary) sides are in/antiphase. At this time, the autonomously operating frequency of the system is stable at 0.809 MHz, which is highly consistent with the resonance frequency of 0.8078 MHz at the maximum amplitude-frequency gain of the system shown in Fig. 10, demonstrating the consistency of theoretical modeling, simulation analysis, and experimental results.

Besides, the experimental waveforms of the primary and secondary dc output currents i_d and i_o are shown in Fig. 18, when the primary and secondary converters operate at a given initial frequency, the similar ac current behavior shown in Fig. 18 is due to the continuous and periodic oscillation of the current when the system is in phase desynchronization. Afterwards, the system self-excited drives converters by following the zero-crossing points of the resonant currents, the dc currents of the system remain constant, achieving phase synchronization of the primary and secondary sides of the system and stable operation at the resonant frequency.

In addition, Fig. 19 shows the experimental waveforms of the output voltages and currents of the primary and secondary

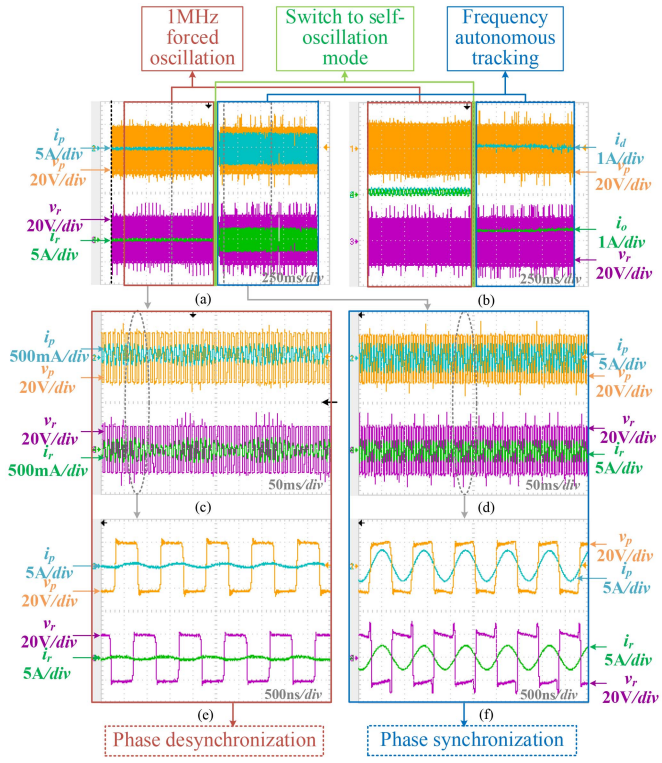

Fig. 20. Experimental waveforms of phase synchronization of the system at the coupling transmission distance of 15 mm. (a) Complete view of the envelopes of v_p, i_p, v_r and i_r. (b) Complete view of the envelopes of v_p, i_d, v_r and i_o. (c) Enlarged view of the fixed-frequency drive stage in Fig. 17(a). (d) Enlarged view of the self-oscillation in Fig. 17(a). (e) Unfolded views at one of the moments in Fig. 17(c). (f) Unfolded views at one of the moments in Fig. 17(d).

converters, as well as the synchronized square wave signal of the output voltage after the zero-crossing comparator, where Fig. 19(a) presents the primary resonant voltage v_p, resonant current i_p, and synchronous voltage signal v_{pz}, while Fig. 19(b) presents the secondary resonant voltage v_r, resonant current i_r, and synchronous voltage signal v_{rz}. It can be clearly seen from that the final output square wave synchronization signals is stable after sampling and zero-crossing comparison of the primary and secondary resonant currents. Meanwhile, the main reason for the slight difference in phase between the synchronous signals and the resonant currents is that the system adds an *RC* lead compensation network during the sampling process of the resonant currents, thereby compensating for the lag delay between the controller and the driver.

In order to further verify the feasibility and effectiveness of phase synchronization method based on self-oscillation mode under coupling capacitances variation, the experimental results with a coupling transmission distance of 15 mm are shown in Fig. 20. Similar to Figs. 17, 18, and 20(a) and (b) present a complete view of the dynamic response and waveforms of resonant voltages, resonant currents, and dc output currents before and after phase synchronization. For the convenience of observation, Fig. 20(c) and (e) provides the enlarged view of the resonant voltages and resonant currents during the initial fixed frequency driving stage. It can be seen that the system is in phase desynchronization at this time, and the resonant currents and dc output currents of the primary and secondary sides are oscillating continuously. The resonant voltage and current of the primary (secondary) converter are not in/antiphase. Fig. 20(d) and (f) shows enlarged views of the resonant voltages and resonant currents after phase synchronization, which is realized by autonomously driving the converters through following the zero-crossing points of the resonant currents. An autonomous operating frequency of the primary and secondary sides remains stable at 0.7948 MHz, which is determined by the maximum amplitude-frequency gain condition of the transfer function matrix and system parameters, consistent with the maximum amplitude-frequency gain point shown in Fig. 11. At this time, the resonant currents and dc currents of the primary and secondary sides tend to stabilize, the resonant voltage and current of the primary (secondary) side remain in/antiphase, achieving phase synchronization under variation on coupling capacitances.

From the above experimental verification and analysis, it can be seen that the proposed phase synchronization method based on self-oscillation mode for the bidirectional EC-WPT system can effectively achieve precise phase synchronization of the primary and secondary sides, and the method is also applicable to the variation on coupling capacitances.

It is noteworthy that some "ringing" and "reverse conduction voltage of the switches" in the experimental results. The main reason for "ringing" is that when the state of the switches changes, due to the existence of parasitic capacitance and inductance, the current of the parasitic inductance changes drastically, resulting in voltage spikes, and the interaction between the parasitic capacitance and the parasitic inductance forms an oscillating loop, leading to oscillating attenuation in the voltage waveforms. Ringing can be effectively improved by reasonably designing the RCD absorption circuit, thereby alleviating high-frequency oscillations and voltage spikes in the circuit. While the reason for "reverse conduction voltage of the switches" is mainly due to the reverse voltage drop caused by negative voltage turning OFF of the switches during dead band period.

VI. Conclusion

This article proposes a phase synchronization method based on self-oscillation mode that can tolerate misalignment of coupling plates for the dual *LCLC*-compensated bidirectional EC-WPT system. The system autonomously drives the converters by following the zero-crossing points of the resonant currents, and ultimately operates at a stable resonant frequency to achieve precise phase synchronization when the transmission distance varies. The effectiveness of the phase synchronization method is verified through simulation and experiment. The main contribution of the proposed phase synchronization method can be concluded as follows.

1) The bidirectional EC-WPT system achieves precise phase synchronization between primary and secondary sides without wireless communication.
2) The proposed phase synchronization method based on self-oscillation mode can track the resonance frequency of the system autonomously and operate stably, which is applicable to the variation on the coupling capacitances,

ensuring the reliability and stability of the system operating at high-frequency.

3) The proposed phase synchronization method is simple in design, easy to implement, high in real-time, and has good anti-interference.

REFERENCES

[1] Q. Xiaodong and S. Yugang, "An overview of electric-filed coupling wireless power transfer technology," *Trans. China Electrotechnical Soc.*, vol. 36, no. 17, pp. 3649–3663, 2021.

[2] H. Zhang and F. Lu, "An improved design methodology of the double-sided LC-compensated EC-WPT system considering the inductance detuning," *IEEE Trans. Power Electron.*, vol. 34, no. 11, pp. 11396–11406, Nov. 2019.

[3] Y. Zhou, X. Wenxun, and Z. Bo, "Qiu Dongyuan. development status of electric-field coupled wireless power transmission technology," *Trans. China Electrotechnical Soc.*, vol. 37, no. 5, pp. 1051–1069, 2022.

[4] L. Huang, A. P. Hu, A. Swain, and Y. Su, "Z impedance compensation for wireless power transfer based on electric field coupling," *IEEE Trans. Power Electron.*, vol. 31, no. 11, pp. 7556–7563, Nov. 2016.

[5] U. K. Madawala and D. J. Thrimawithana, "A bidirectional inductive power interface for electric vehicles in V2G systems," *IEEE Trans. Ind. Electron.*, vol. 58, no. 10, pp. 4789–4796, Oct. 2011.

[6] Nguyen B. X. et al., "An efficiency optimization scheme for bidirectional inductive power transfer systems," *IEEE Trans. Power Electron.*, vol. 30, no. 11, pp. 6310–6319, Nov. 2015.

[7] S. Min, D. Xin, L. Yanling, and S. Yugang, "Research status of bidirectional wireless power transfer technology," in *Proc. CSEE*, 2023, pp. 1–19.

[8] X. Dai, M. Sun, P. Deng, R. Wang, and Y. Su, "Asymmetric bidirectional capacitive power transfer method with push-pull full-bridge hybrid topology," *IEEE Trans. Power Electron.*, vol. 37, no. 11, pp. 13902–13913, Nov. 2022.

[9] L. Yang, M. Ju, and B. Zhang, "Bidirectional undersea capacitive wireless power transfer system," *IEEE Access*, vol. 7, pp. 121046–121054, 2019.

[10] P. J. Vishnu and N. R. Tummuru, "A phase shift control strategy for bidirectional power flow in capacitive wireless power transfer system using LCLC compensation," in *Proc. IEEE Int. Conf. Power Electron., Smart Grid Renewable Energy*, Cochin, India, 2020, pp. 1–6.

[11] M. Sun, X. Dai, Y. Su, Y. Li, and S. Zhao, "Frequency and phase synchronous control method without communication of the BCPT system," *IEEE Trans. Power Electron.*, vol. 39, no. 4, pp. 4792–4804, Apr. 2024.

[12] D. J. Thrimawithana, U. K. Madawala, and M. Neath, "A synchronization technique for bidirectional IPT systems," *IEEE Trans. Ind. Electron.*, vol. 60, no. 1, pp. 301–309, Jan. 2013.

[13] T. Tan, K. Chen, Y. Jiang, Q. Lin, L. Yuan, and Z. Zhao, "A bidirectional wireless power transfer system control strategy independent of real-time wireless communication," *IEEE Trans. Ind. Appl.*, vol. 56, no. 2, pp. 1587–1598, Feb. 2020.

[14] D. Zhang, M. Chen, B. Li, X. Wang, X. Sun, and F. Jiang, "Synchronization strategy based on resonant current detection for bidirectional wireless charging system," *IEEE Trans. Power Electron.*, vol. 37, no. 9, pp. 11436–11449, Sep. 2022.

[15] F. Liu, K. Li, K. Chen, and Z. Zhao, "A phase synchronization technique based on perturbation and observation for bidirectional wireless power transfer system," *IEEE J. Emerg. Sel. Topics Power Electron.*, vol. 8, no. 2, pp. 1287–1297, Jun. 2020.

[16] Y. Tang, Y. Chen, U. K. Madawala, D. J. Thrimawithana, and H. Ma, "A new controller for bidirectional wireless power transfer systems," *IEEE Trans. Power Electron.*, vol. 33, no. 10, pp. 9076–9087, Jun. 2018.

[17] F. Lu, H. Zhang, H. Hofmann, and C. Mi, "A double-sided LCLC compensated capacitive power transfer system for electric vehicle charging," *IEEE Trans. Power Electron.*, vol. 30, no. 11, pp. 6011–6014, Nov. 2015.

[18] C. S. Tang, Y. Sun, Y. G. Su, S. K. Nguang, and A. P. Hu, "Determining multiple steady-state ZCS operating points of a switch-mode contactless power transfer system," *IEEE Trans. Power Electron.*, vol. 24, no. 2, pp. 416–425, Feb. 2009.

[19] Y. Fei, F. Chen, R. Gao, S. Zhao, C. Tang, and L. Zhao, "Oscillation frequency manipulation in autonomous WPT systems with series–series compensation," *IEEE Trans. Power Electron.*, vol. 39, no. 1, pp. 58–63, Jan. 2024.

Min Sun received the B.E. degree in automation from the College of Artificial Intelligence, Chongqing Technology and Business University, Chongqing, China, in 2017, and the Ph.D. degree in control theory and control engineering from Chongqing University, Chongqing, China, in 2024.

Since 2024, she has been with the Faculty of Electrical and Automation Engineering, East China Jiaotong University, Jiangxi, China. Her current research interests include the bidirectional wireless power transfer and power electronics.

Xin Dai (Member, IEEE) received the B.S. degree in industrial automation from Yuzhou University, Chongqing, China, in 2000, and the Ph.D. degree in control theory and control engineering from the School of Automation, Chongqing University, Chongqing, China, in 2006.

In 2012, he was a Visiting Scholar with The University of Auckland, Auckland, New Zealand. He is currently a Professor with the School of Automation, Chongqing University. His research interests include inductive power transfer technology and nonlinear dynamic behavior analysis of power electronics.

Pengqi Deng received the B.E. degree in automation and the Ph.D. degree in control theory and control engineering from the College of Automation, Chongqing University, Chongqing, China, in 2015 and 2024, respectively.

Since 2024, he has been with the College of Optoelectronics Engineering, Chongqing University of Posts and Telecommunications, Chongqing, China, where he is currently a Postdoctor. His research interests include nonlinear modeling and analysis, electromagnetic interference suppression, and wireless power transfer.

Shijun Zhao was born in Sichuan, China. He received the B.Eng. degree in automation from the Faculty of Information Engineering and Automation, Kunming University of Science and Technology, Yunnan, China, in 2017. He is currently working toward the Ph.D. degree in control theory and control engineering with Chongqing University, Chongqing, China.

His current research interests include modeling, system identification and control methods of wireless power transfer, and power electronics.

Yanling Li received the Ph.D. degree in control theory and control engineering from the School of Automation, Chongqing University, Chongqing, China, in 2017.

She is currently with the School of Electrical Engineering and Electronics Information, Xihua University, Chengdu, China. Her research interests include wireless power transfer and advanced control technology in power electronics.